Characterization of Nanostructured Titanates Obtained by Alkali Treatment of TiO_2-Anatases with Distinct Crystal Sizes

Edisson Morgado, Jr.,*[,†,‡] Marco A. S. de Abreu,[†] Gustavo T. Moure,[†] Bojan A. Marinkovic,[§] Paula M. Jardim,[§] and Antonio S. Araujo[‡]

PETROBRAS S.A./CENPES, Research and Development Centre, Cidade Universitaria, Avenida Jequitiba, 950, 21941-598, Rio de Janeiro-RJ, Brazil, Department of Materials Science and Metallurgy, Pontifical Catholic University, C.P.: 38008, 22453-900 Rio de Janeiro-RJ, Brazil, and Department of Chemistry, University of Rio Grande do Norte, CP 1662, 59078-970, Natal-RN, Brazil

Received June 2, 2006. Revised Manuscript Received December 5, 2006

Layered titanate nanotubes (TTNT) with a general formula $Na_xH_{2-x}Ti_3O_7 \cdot nH_2O$ were synthesized by hydrothermally reacting TiO_2-anatase with NaOH at 120 °C. Detailed TGA and XRD characterization indicated that the as-synthesized material rich in sodium as an interlayer cation contained intercalated water (n), which was reduced substantially after nearly complete proton exchange ($x = \sim 0$), while the interlayer distance decreased approaching the interlayer distance d_{200} of $H_2Ti_3O_7$. Chemical composition and crystal structure of TTNT as well as their dependence on sodium content were not affected by the crystallite size of the starting anatase. On the other hand, TEM examination and N_2 adsorption measurements revealed distinct morphology at the nanometer scale and different textural properties depending on the precursor TiO_2. Such dependence was rationalized based on a dissolution−recrystallization mechanism.

1. Introduction

Nanostructured TiO_2 materials have been extensively researched due to their potential applications in semiconductor devices,[1] electrodes for lithium batteries,[2] dye-sensitized solar cells,[3] photocatalysts,[4] and catalyst supports,[5] to which the crystalline phase state, surface area, pore size distribution, and morphology are crucial properties for their enhanced performance.

TiO_2-derived nanotubes obtained by an alkali treatment without using any template molds have attracted a great deal of attention since the innovative work of Kasuga et al.,[6,7] due to the simplicity of the synthesis and to the fact that long nanotubes with an external diameter as small as 10 nm can be obtained. This material can be easily fabricated by hydrothermal treatment of crystalline TiO_2 in highly concentrated NaOH aqueous solution at moderate temperatures (90−170 °C). Many groups have tried to modify the process and to elucidate the mechanism of formation as well as the true composition and crystalline structure of the resulting titania or titanate nanotubes (TTNT).

Apparently, there is a common agreement that after the breaking of chemical bonds in the starting 3-D TiO_2 structure, planar entities (2-D) are formed and converted into nanotubes (1-D) through a sheet folding[8−16] or wrapping[17] mechanism. Other than the original assumption of Kasuga[7] that acid washing of the precipitate after hydrothermal treatment was essential for sodium exchange with a consequent formation of TTNT, most researchers have found that nanotubes are formed earlier during the hydrothermal alkali reaction.[10,12,18−23]

* Corresponding author. Tel.: +55 21 3865 6716. Fax: +55 21 3865 6626. E-mail: emorgado@petrobras.com.br.
† Petrobras R & D Center.
‡ University of Rio Grande do Norte.
§ Pontifical Catholic University.

(1) (a) Fujishima, K.; Yamada, I. *J. Phys. Chem.* **1993**, *97*, 619. (b) Hoyer, P. *Langmuir* **1996**, *12*, 1411.
(2) (a) Kavan, L.; Kalbac, M.; Zukalova, M.; Exnar, I.; Lorezen, V.; Nesper, R.; Graetzel, M. *Chem. Mater.* **2004**, *16*, 477. (b) Gao, X. P.; Lan, Y.; Zhu, H. Y.; Liu, J. W.; Ge, Y. P.; Wu, F.; Song, D. Y. *Electrochem. Solid-State Lett.* **2005**, *8*, 26.
(3) Michailowski, A.; Almawlawi, D.; Cheng, G.; Moskovits, M. *Chem. Phys. Lett.* **2001**, *349*, 1.
(4) (a) Adesina, A. A. *Catal. Surv. Asia* **2004**, *8*, 265. (b) Adachi, M.; Murata, Y.; Harada, M.; *Chem. Lett.* **2000**, *8*, 942.
(5) (a) Idakiev, V.; Yuan, Z.-Y.; Tabakova, T.; Su, B. -L. *Appl. Catal., A* **2005**, *28*, 149. (b) Lin, C.-H. et al. *Catal. Lett.* **2004**, *98*, 61. (c) Bavykin, D. V.; Lapkin, A. A.; Plucinsky, P. K.; Friedrich, J. M.; Walsh, F. C. *J. Catal.* **2005**, *235*, 10.
(6) Kasuga, T.; Hiramatsu, M.; Hoson, A.; Sekino, T.; Niihara, K. *Langmuir* **1998**, *14*, 3160.
(7) Kasuga, T.; Hiramatsu, M.; Hoson, A.; Sekino, T.; Niihara, K. *Adv. Mater.* **1999**, *11*, 1307.
(8) Wang, Y. Q.; Hu, G. Q.; Duan, X. F.; Sun, H. L.; Xue, Q. K. *Chem. Phys. Lett.* **2002**, *365*, 427.
(9) Ma, R.; Bando, Y.; Sasaki, T.; *Chem. Phys. Lett.* **2003**, *380*, 577.
(10) Chen, Y.-F.; Lee, C.-Y.; Yeng, M.-Y.; Chiu, H.-T. *Mater. Chem. Phys.* **2003**, *81*, 39.
(11) Yao, B. D.; Chan, Y. F.; Zhang, X. Y.; Zhang, W. F.; Yang, Z. Y.; Wang, N. *Appl. Phys. Lett.* **2003**, *82*, 281.
(12) Wang. W.; Varghese, O. K.; Paulose, M.; Grimes, C. A. *J. Mater. Res.* **2004**, *19*, 417.
(13) Yuan, Z.-Y.; Su, B.-L. *Colloids Surf., A* **2004**, *241*, 173.
(14) Ma, R.; Fukuda, K.; Sazaki, T.; Osada, M.; Bando, Y. *J. Phys. Chem. B* **2005**, *109*, 6210.
(15) Thorne, A.; Kruth, A.; Tunstall, D.; Irvine, J. T. S.; Zhou, W. J. *Phys. Chem. B* **2005**, *109*, 5439.
(16) Zhang, S.; Chen, Q.; Peng, L.-M. *Phys. Rev. B: Condens. Matter* **2005**, *71*, 014104.
(17) Bavykin, D. V.; Parmon, V. N.; Lapkin, A. A.; Walsh, F. C. *J. Mater. Chem.* **2004**, *14*, 3370.
(18) Du, G. H.; Chen, Q.; Che, R. C.; Yuan, Z. Y.; Peng, L.-M. *Appl. Phys. Lett.* **2001**, *79*, 3702.
(19) Seo, D.-S.; Lee, J. K.; Kim, H. *J. Cryst. Growth* **2001**, *229*, 428.
(20) Chen, Q.; Zhou, W.; Du, G.; Peng, L.-M. *Adv. Mater.* **2002**, *14*, 1208.
(21) Nakahira, A.; Kato, W.; Tamai, M.; Isshiki, T.; Nishio, K. *J. Mater. Sci.* **2004**, *39*, 4239.

10.1021/cm061294b CCC: $37.00
Published on Web 01/25/2007

Different crystal structures and compositions have been proposed to describe the TTNT structure, such as TiO_2-anatase,[6,8,11,12,24,25] $Na_xH_{2-x}Ti_2O_4(OH)_2$,[22] trititanates $H_2Ti_3O_7$,[13,15,18,20,26] $H_2Ti_3O_7{\cdot}nH_2O$,[27] $Na_xH_{2-x}Ti_3O_7$,[17,28−29] tetratitanate $H_2Ti_4O_9{\cdot}H_2O$,[21,30] and lepidocrocite titanate $H_xTi_{2-x/4}\square_{x/4}O_4$.[9,14] A bititanate structure, $H_2Ti_2O_5{\cdot}H_2O$, has been recently claimed as well;[31] however, when one calculates its bond lengths: $bl = ((a(x_i - x_j))^2 + (b(y_i - y_j))^2 + (c(z_i - z_j))^2)^{0.5}$ based on the atomic coordinates (x_i,y_i,z_i) and cell parameters (a,b,c) supplied in the paper, physically impossible distances are obtained: Ti−O (1.3−1.5 Å) and O−O (0.2 Å), thus ruling out this option. In our previous paper,[23] we showed strong evidence to state that TTNT actually possesses a trititanate structure with a general formula $Na_xH_{2-x}Ti_3O_7{\cdot}nH_2O$, where x and n depend on the degree of sodium proton exchange during the washing procedure, which has recently been corroborated by Ferreira et al.[32]

The main variables in this soft-chemistry process are reaction temperature, caustic concentration, and the type of TiO_2 as a raw material. It is well-established that hydrothermal temperature should be within the range of 90−170 °C inasmuch as lower temperatures will impair TiO_2 conversion within practical reaction times, whereas higher temperatures may lead to distinct nanoparticle shapes (e.g., nanofibers, belts, or ribbons) other than nanotubes.[13,14,17] It is also well-documented, although not so well-explained, that optimum caustic concentration for maximum TTNT yield is around 10 mol/L.[6,13] In contrast, the effect of the starting TiO_2, which can be in the form of anatase, rutile, or amorphous titania, on the morphology of the resulting TTNT is rather controversial.

Some authors reported that TTNT could not be produced from amorphous titania.[11,13,20] In fact, all successful syntheses of titanate nanotubes reported in literature via this chemical method applied anatase, rutile, or mixture of both as a raw material. An exception has been recently reported by Wu et al.,[33] who claimed to have obtained TTNT from amorphous titanium oxide. Confirming Kasuga's finding, other researchers[2,15,34] have recently reported the abundant formation of TTNT from rutile, in disagreement with Chen et al.,[10] who could not observe nanotubes in a significant amount when anatase was replaced by rutile. Seo et al. and Nakahira et al.[19,21] found lower rates in nanotube formation when using rutile in comparison with anatase, which was tentatively rationalized by Seo et al. in terms of the higher asymmetry in anatase crystals. To make it more divergent, Wen et al.[35] reported a clear formation of nanotubes when rutile was used as a starting TiO_2; but when anatase was used instead, they found that the formation of nanofibers was favored in to the detriment of nanotubes. Inversely, Susuki et al.[36] could only obtain nanofibers (not TTNT) from natural rutile sands. It seems obvious that some other parameter, besides the TiO_2 crystalline form, is playing a role.

Some authors evidenced the effect of the particle size of the starting TiO_2 on the rate of nanotube formation. Ma et al.[30] observed lower rates starting from larger anatase particles (200 vs 10 nm), and Nakahira et al.[21] showed that differences in reactivity toward TTNT were more related to the particle size of the starting TiO_2 than to its crystalline phase. According to some authors,[13,26,28] the dimensions of TTNT obtained via Kasuga's method varied within very narrow ranges (diameters: internal 2−7 nm and external 5−10 nm) and were independent of the particle size of the starting TiO_2. However, Zhang et al.[24] concluded that the morphology and surface area of TTNT were influenced by both crystalline phase and particle size of the starting TiO_2; ultrafine rutiles led to TTNT with longer lengths, while ultrafine anatase led to less uniform nanotubes. Yuan and Su[13] and Idakiev et al.[5a] verified that starting anatase with a smaller crystal size led to TTNT with a higher surface area.

Despite the considerable number of papers dealing with the influence of the starting TiO_2 on the rate of its conversion into TTNT and the yields of nanotubes, there is a lack of deeper investigation about the effects on the TTNT characteristics. Analysis of the morphological properties of produced TiO_2 nanotubes is usually based exclusively on electron microscopy imaging, where the properties of a limited number of nanotubes are evaluated, and statistically representative data may not be reached.

The purpose of this work is to shed more light on this subject by detailed characterization of titanate nanotubes produced from two anatase sources with different average crystal sizes via hydrothermal alkali treatment. A combination of scanning (SEM) and transmission microscopy imaging (TEM) with nitrogen adsorption methods was applied for elucidation of the textural properties, while X-ray diffraction (XRD), flame photometry, and thermal analysis (TG/DTA) completed the picture on crystal structure and composition. Since our earlier study demonstrated an important effect of structural sodium on some TTNT properties,[23] the present comparison has been made on TTNT samples within a range of distinct sodium contents, according to the applied washing step.

2. Experimental Procedures

2.1. TiO_2-Anatase Raw Materials. Two commercial TiO_2-anatase powders with remarkably distinct crystallinity were used

(22) Yang, J.; Jin, Z.; Wang, X.; Li, W.; Zhang, J.; Zhang, S.; Guo, X.; Zhang, Z. *Dalton Trans.* **2003**, *20*, 3898.
(23) Morgado, E., Jr.; Abreu, M. A. S.; Pravia, O. R. C.; Marinkovic, B. A.; Jardim, P. M.; Rizzo, F. C.; Araujo, A. S. *Solid State. Sci.* **2006**, *8*, 888.
(24) Zhang, Q.; Gao, L.; Sun, L.; Zheng, S. *Chem. Lett.* **2002**, 226.
(25) Qian, L.; Du, Z.-L.; Yang, S.-Y.; Jin, Z.-S. *J. Mol. Struct.* **2005**, *749*, 103.
(26) Chen, Q.; Du, G.; Zhang, S.; Peng, L.-M. *Acta Crystallogr., Sect. B* **2002**, *58*, 587.
(27) Suzuki, Y.; Yoshikawa, S. *J. Mater. Res.* **2004**, *19*, 982.
(28) Sun, X.; Li, Y. *Chem.−Eur. J.* **2003**, *9*, 2229.
(29) Yoshida, R.; Suzuki, Y.; Yoshikawa, S. *Mater. Chem. Phys.* **2005**, *91*, 409.
(30) Ma, Y.; Lin, Y.; Xiao, X.; Zhou, X.; Li, X. *Mater. Res. Bull.* **2006**, *41*, 237.
(31) Tsai, C-C.; Teng H. *Chem. Mater.* **2006**, *18*, 367.
(32) Ferreira, O. P.; Souza Filho, A. G.; Mendes Filho, J.; Alves, O. L. *J. Braz. Chem. Soc.* **2006**, *17*, 393.
(33) Wu, D.; Liu, J.; Zhao, X.; Li, A.; Chen, Y.; Ming, N. *Chem. Mater.* **2006**, *18*, 547.
(34) Tsai, C.-C.; Teng, H. *Chem. Mater.* **2004**, *16*, 4352.
(35) Wen, B.; Liu, C.; Liu, Y.; Zhang, Z. *J. Nanosci. Nanotechnol.* **2004**, *4*, 1062.
(36) Suzuki, Y.; Pavasupree, S.; Yoshikawa, S. *J. Mater. Res.* **2005**, *20*, 1063.

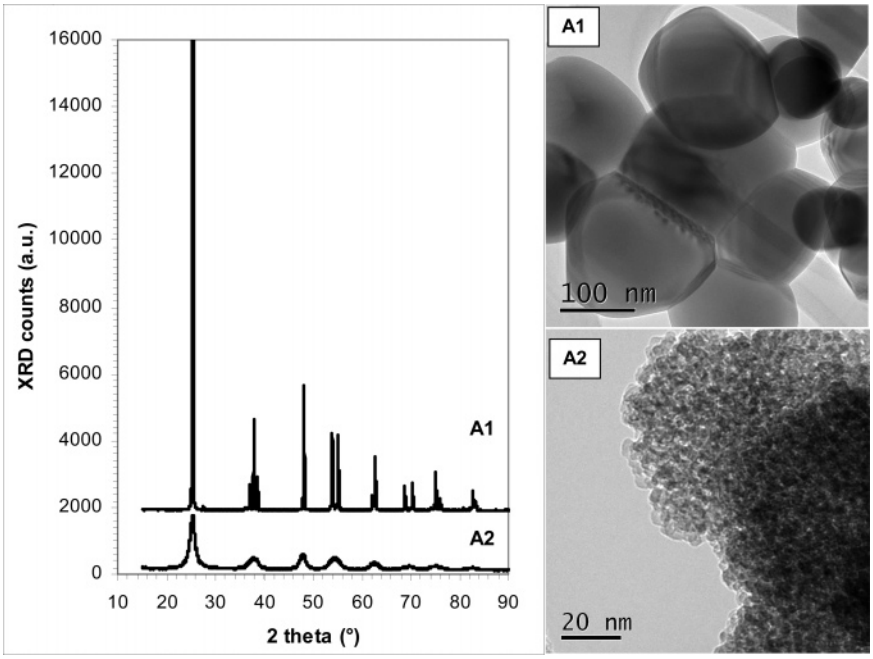

Figure 1. XRD patterns and transmission electron microscopy images of the starting TiO_2-anatase powders A1 and A2.

Table 1. Water Loss Determined by TGA of TTNT Samples with Different Sodium Contents Prepared from Different Anatase Sources and Their Corresponding Calculated *x* and *n* Assuming the Trititanate Composition = $Na_xH_{2-x}Ti_3O_7 \cdot nH_2O$

			% water wt loss by TGA				
sample/ starting anatase	reaction condition	wt % Na (as such)	physisorbed (25−100 °C)	chemisorbed cor (100−500 °C)[a]	% H_2O interlayer/ structural	*x*	*n*
TTNT-1/A1	120 °C/30 h	0.2	4.4	6.8	0.0/6.9	0.0	0.0
TTNT-2/A1	120 °C/30 h	1.2	10.3	8.2	2.0/6.2	0.2	0.3
TTNT-3/A1	120 °C/30 h	4.1	7.3	7.0	2.1/4.9	0.5	0.3
TTNT-4/A1	120 °C/30 h	6.4	9.6	8.1	4.6/3.5	0.9	0.7
TTNT-5/A1	120 °C/30 h	9.5	10.0	8.8	7.1/1.7	1.4	1.2
TTNT-1/A2	120 °C/15 h	0.3	7.8	8.2	1.4/6.8	0.0	0.2
TTNT-2/A2	120 °C/30 h	0.5	6.9	7.7	1.0/6.7	0.1	0.2
TTNT-3/A2	120 °C/30 h	3.7	7.9	7.7	2.7/5.0	0.5	0.4
TTNT-4/A2	120 °C/15 h	4.8	4.7	8.3	4.3/4.0	0.7	0.7
TTNT-5/A2	120 °C/15 h	9.5	7.9	8.1	6.2/1.9	1.4	1.0

[a] Percent of chemisorbed water corrected by excluding contribution of physisorbed water from the total mass.

in this study: A1 (Tiona AT1, supplied by Millenium) and A2 (FINNTi -S140, supplied by Kemira). Their X-ray diffraction patterns and TEM images are shown in Figure 1. Their estimated average crystal sizes based on the Scherrer equation were, respectively, 220 and 8 nm, in good agreement with their corresponding morphologies revealed by TEM (Figure 1). BET surface areas of 7 and 150 m^2/g were, respectively, measured via N_2 adsorption at −196 °C, after pretreatment of samples A1 and A2 at 300 °C.

2.2. Synthesis of TTNT. Anatase powders A1 and A2 (∼3 g on a TiO_2 basis) were separately dispersed in 50 mL of a NaOH solution at three different concentrations (10, 15, and 20 M); the six mixtures were charged to stainless steel Parr bombs (model A-500) equipped with electrical resistance heating, temperature control, and a magnetic stirrer. The reactors were sealed and heated to 120 °C, and the mixtures were left stirring at this condition for 15 and 30 h. Each collected precipitate was filtered, resuspended with 600 mL of HCl 0.1 M solution at pH 4.5, and filtered again; the process was repeated three times, and finally, the precipitate was washed with 600 mL of deionized water and dried overnight in an air-circulating oven at 120 °C. The resulting white powder was analyzed by XRD, flame photometry, and electron microscopy. This first set was designed to determine for each starting anatase the corresponding reaction condition at which complete conversion would be achieved, as discussed in the following section. Then, new preparations were carried out with A1 and A2 reacting under constant optimal conditions (NaOH 10 M, 120 °C for 15−30 h) to collect enough TTNT material for this work. The as-synthesized precipitate in each case was divided into different parts, each one undergoing the same washing/drying steps described previously but being washed either just with deionized water or with an HCl solution at different pH values ranging from 7.0 to 1.0, thus producing the corresponding TTNT/A1 and TTNT/A2 series samples with sodium levels ranging from 0.2 to ca 10% Na (Table 1).

2.3. Characterization Tools. Sodium content was measured on an as-such (dried) basis by flame photometry after dissolving TTNT in concentrated H_2SO_4; % Na was determined after proper calibration with standards. X-ray diffraction (XRD) analyses were performed on a powder diffractometer (Rigaku XRD-6000), operating with Cu Kα radiation at 40 kV and 35 mA, scan speed of 0.24°/min, step size of 0.02°, and preset time of 5 s. The values of interlayer distances and their error bars were calculated through single line fitting with fundamental parameters using Topas-Academic; such an approach intrinsically corrects for errors in the 2θ position due to instrument and sample aberrations. Scanning electron microscopy (SEM) images were recorded on Au-metallized powder samples with a Shimadzu SSX-550 Superscan, operating at an accelerating voltage of 30 kV. Transmission electron microscopy (TEM) images and selected area electron diffraction

(SAED) were recorded using a Gatan CCD camera on a JEOL-2010 microscope operating at 200 kV. Specimens for TEM observation were prepared by dispersing the powder in alcohol by ultrasonic treatment, then dropping the solution onto a holey carbon film supported by a copper grid. Chemical composition of individual nanotubes was examined via energy-dispersive X-ray spectroscopy (TEM/EDS). Shimadzu instruments were used to carry out thermogravimetry (TGA51-H) and differential thermal analyses (DTA-50) in dry air flow (50 mL/min); the temperature range was 25−800 °C with a heating-up rate of 5 °C/min. Textural properties of the powder samples, pretreated at 120 °C under vacuum down to 50 mTorr, were characterized by N_2 adsorption at −196 °C on a Micromeritics TriStar 3000 V6.03 instrument. Specific surface area was calculated by using the classic BET equation in the P/P_o range of 0.06−0.21, and the pore volume distribution within the 2−60 nm diameter range was determined by means of the Barrett−Joyner−Halenda (BJH) algorithm method using the desorption branch of the isotherm.

3. Results and Discussion

3.1. Reaction Conditions for Complete Conversion of A1 and A2. Samples obtained in the first experimental set ended up with approximately the same sodium content (∼4 wt % Na). Their XRD patterns in Figure 2a,b shows that A2 could be completely converted into a titanate structure with its typical strong diffraction peak around $2\theta = 10°$ attributed to the interlayer distance, after hydrothermal treatment at 120 °C for 15 h in the presence of NaOH 10−15 M. At this temperature, A1 with its strong and fine peak at 25° 2θ could only be completely converted into a layered titanate either after extended reaction time (30 h) with NaOH 10 M or after 15 h with a more concentrated caustic (NaOH 15 M). Reaction of both A1 and A2 with NaOH in excess (20 M) led to an amorphous product. These findings could be confirmed by scanning and transmission electron microscopy as well as electron diffraction (SAED) examination. It was evident that precursor A2 lost its original crystal structure under reaction conditions faster than A1. To guarantee complete conversion of the reactant, the minimum reaction times established for alkali treatment of A1 and A2 with NaOH 10 M at 120 °C were 30 and 15 h, respectively. Table 1 summarizes the group of samples so obtained according to their precursor anatase and sodium content after washing. Hereafter, a detailed characterization of these TTNT samples is presented and discussed.

3.2. Morphological Properties. SEM images of the as-synthesized samples revealed that regardless the anatase source, the starting spherical titania particles were completely transformed into a fibrous and very porous aggregated material (Figure 3). It was not possible through this technique to identify nanotubes nor to make a reliable distinction with respect to morphological features between products obtained from different anatase sources, irrespective of their sodium content. All samples showed numerous long fibers, some micrometers in length and approximately 30−80 nm in width, usually stuck together or arranged in a woven network.

When observed by TEM, all products showed the formation of multi-walled nanotubes, generally opened at both ends, either randomly oriented or as aligned bunches, coexisting more or less with layered sheets or incompletely rolled-up tubes. However, there were evident differences with respect to the yields of nanotubes and their dimensions, depending on the anatase source. Nanotubes synthesized from anatase A1 were very similar in their dimensions with external (internal) diameters ranging from 6 to 11 (3 to 5)

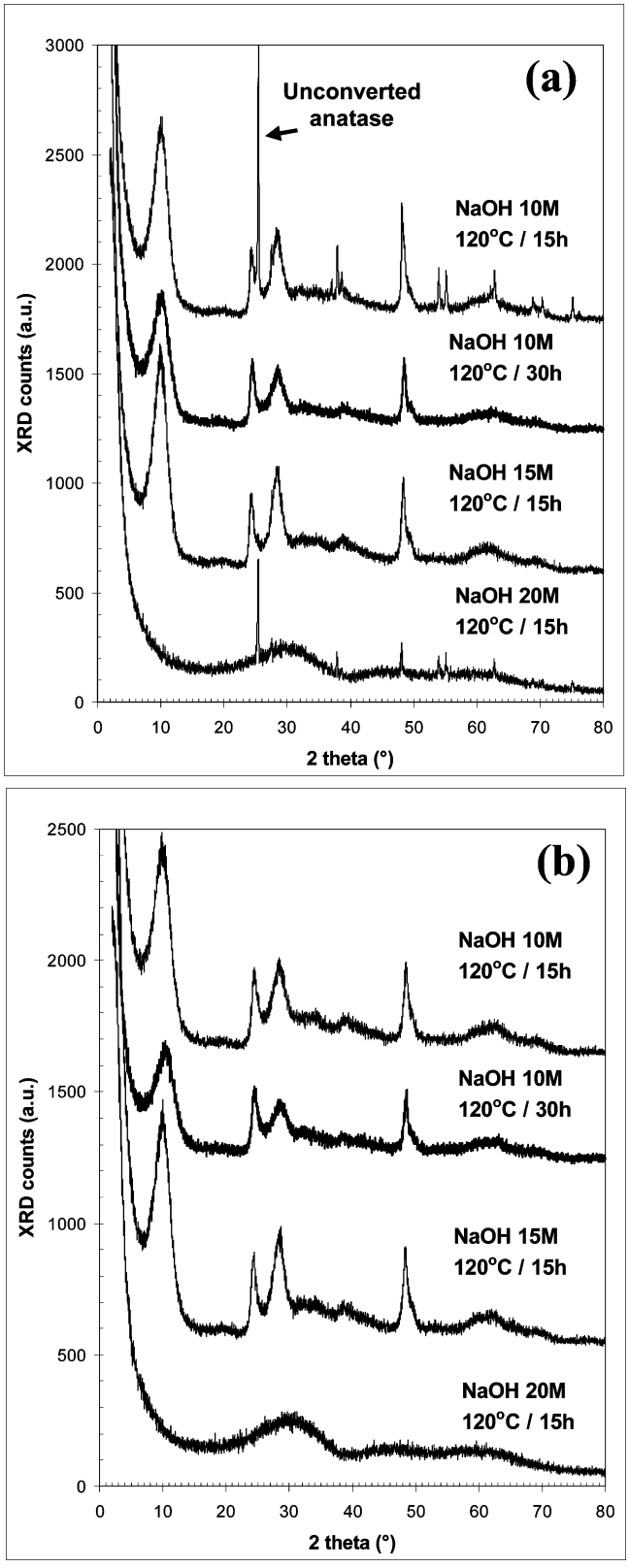

Figure 2. XRD patterns of products from alkali hydrothermal treatment of (a) A1 and (b) A2, at different NaOH concentrations and reaction conditions.

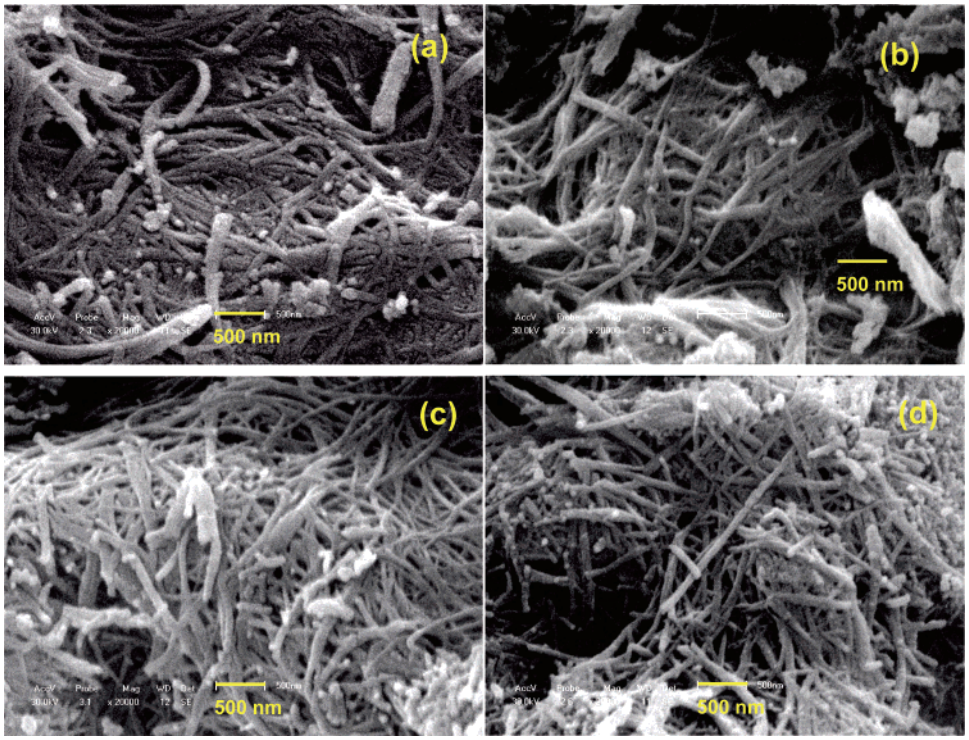

Figure 3. SEM images of TTNT samples (a) TTNT/A1, high sodium; (b) TTNT/A1, low sodium; (c) TTNT/A2, high sodium; and (d) TTNT/A2, low sodium.

nm, walls of three to five layers, and length of several hundreds of nanometers, independently of the sodium content (Figure 4a−c). In contrast, TTNT samples obtained from A2 visually showed lower yields of well-defined nanotubes, but whenever found, they were systematically and significantly larger than those found in the TTNT-A1 series, with external (internal) diameters ranging from 10 to 30 (4 to 10) nm (Figure 4d−f) and thicker walls containing higher numbers of layers. As illustrated in Figure 4e, nanotubes in TTNT-A2 samples coexist with larger amounts of poorly defined entities, not necessarily planar but most likely incompletely curved into nanotubes. Sometimes, an assumed nanotube might be alternatively interpreted as a nanosheet with two brims curved (Figure 4f). However, tilting experiments during TEM observation have been made and proved the existence of nanotubular shapes in several cases. It is worth mentioning that even with an extended reaction time up to 30 h, the material synthesized from A2 did not improve significantly the yield of nanotubes, although nanotubes with smaller diameters could be found coexisting with bigger ones and lots of slightly curved sheets. These morphological differences between TTNT-A1 and TTNT-A2 will be very important when discussing the textural properties of these materials as measured by N_2 adsorption.

TEM/EDS analysis of individual nanotubes clearly detected sodium on those TTNT samples with higher than 2 wt % Na; otherwise, the sodium peak could hardly be noticed in the EDS spectra as it was approaching the detection limit. All sodium measured in the bulk by flame photometry was assumed to belong to the TTNT structure since intensive washing has been applied to remove all sodium hydroxide in excess.

3.3. XRD Properties. Figure 5 shows the XRD patterns of the as-synthesized TTNT samples. The main diffraction peaks are typical of layered titanates, especially the strong broad one around $2\theta = 10°$, attributed to the interlayer distance in $Na_xH_{2-x}Ti_3O_7{\cdot}H_2O$.[23,27,32] The position of this peak slightly shifted so that the interlayer distance could be related to the sodium content (Figure 6). Although relatively small differences are involved, the lower the sodium content, the shorter the interlayer distance was. The graph in Figure 6 indicated a nonlinear dependence and that this was not influenced by the starting anatase used for the TTNT syntheses. The interlayer distance varied between 0.80 and 0.90 nm, somewhat above the *d* values of 0.78 and 0.84 nm in bulk trititanates $H_2Ti_3O_7$ and $Na_2Ti_3O_7$, respectively, thus confirming the indication of intercalated water being responsible for the interlayer expansion. On the other hand, the extrapolation to null sodium in Figure 6 seems to point to an interlayer distance of 0.78 nm, which is quite close to the *d* value of the fully protonic trititanate $H_2Ti_3O_7$. Another clear feature, also independent of the starting TiO_2, was the significant weakening of the peaks at $2\theta = \sim 10$ and 28.5° when sodium was reduced to almost complete proton exchange (0.2−0.3% Na in Figure 5), confirming previous observations.[23,28]

3.4. Thermogravimetric Analyses—TTNT Compositions. The total weight loss of the TTNT samples, ascribed only to H_2O release, ranged from 11 to 18% with no significant loss occurring at temperatures above 500 °C. TGA reproducibility tests showed that the amount of water lost below 100 °C varied randomly depending on the atmosphere and time at which the dried TTNTs were submitted during storage, whereas the weight loss between 100 and 500 °C

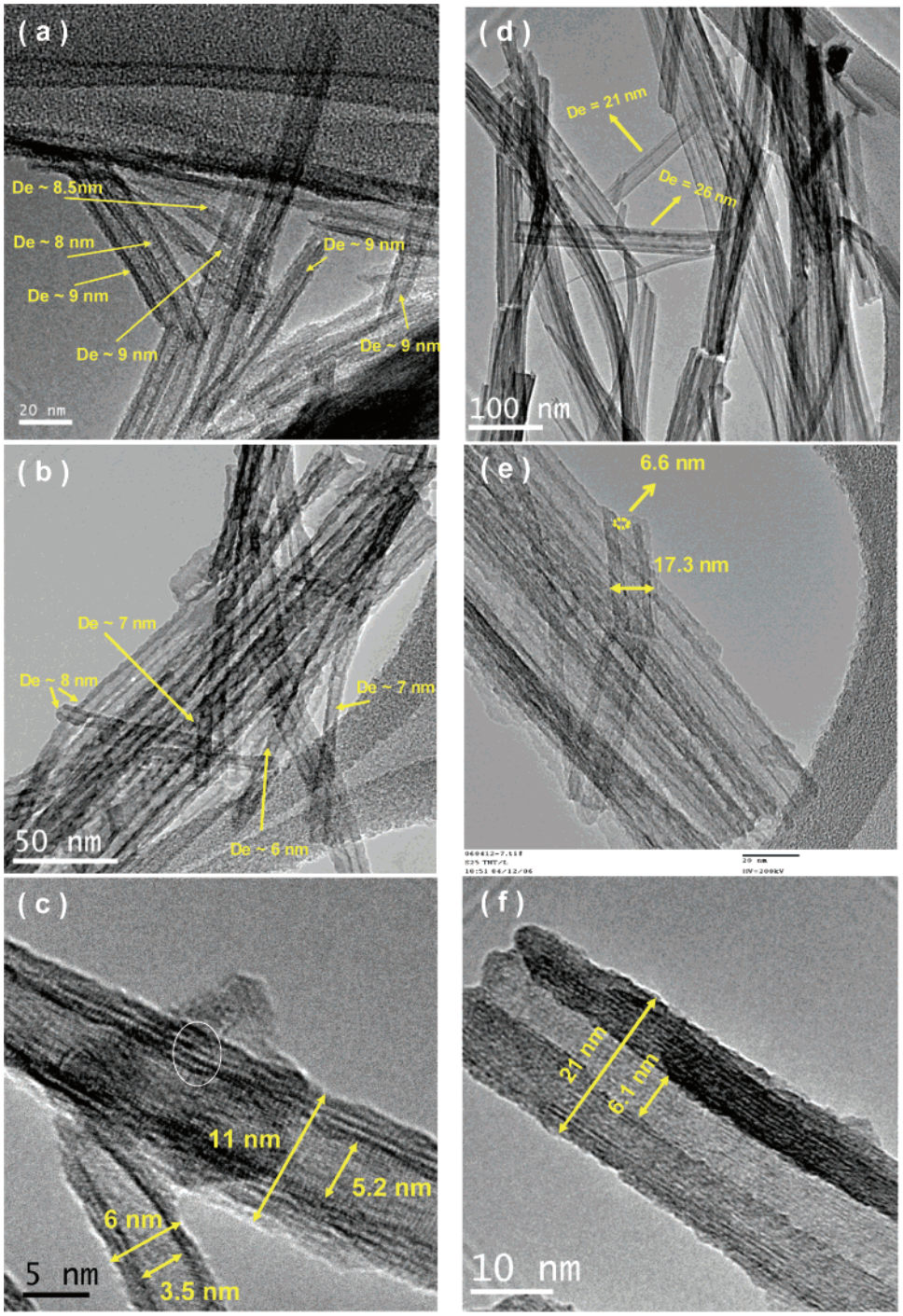

Figure 4. TEM images of TTNT samples (a and c) TTNT/A1, high sodium; (b) TTNT/A1, low sodium; (d and f) TTNT/A2, high sodium; and (e) TTNT/A2, low sodium.

remained quite reproducible. The former is due to air moisture physically adsorbed at the surface of the as-prepared samples providing no relevant information about TTNT structural composition, so that only the losses above 100 °C have been taken into account to assess the TTNT composition. As the weight percentage lost between 100 and 500 °C determined by TGA was relative to the total amount of released water, a correction had to be applied by excluding the contribution of physisorbed water to obtain the actual percentage of chemically bound water in the structure. As shown in Table 1, this value was between 7 and 9 wt %, which is slightly above the theoretical loss of ~7.0 wt % for the thermal decomposition of $H_2Ti_3O_7 = > 3TiO_2 + H_2O$. As trititanates containing sodium in the structure ($Na_xH_{2-x}Ti_3O_7$) would theoretically have to release less than 7% of structural water, one must conclude that our TTNTs with layered trititanate crystals should possess chemically bound H_2O in its stoichiometry, intercalated between crystal layers. The corrected percentage of water lost between 100 and 500 °C can hence be assigned to interlayer H_2O besides structural water (-OH). By taking into account this value and the sodium content, as well as assuming the hydrated trititanate composition: $Na_xH_{2-x}Ti_3O_7 \cdot nH_2O$, one could estimate the values of x and n, thus determining the chemical composition

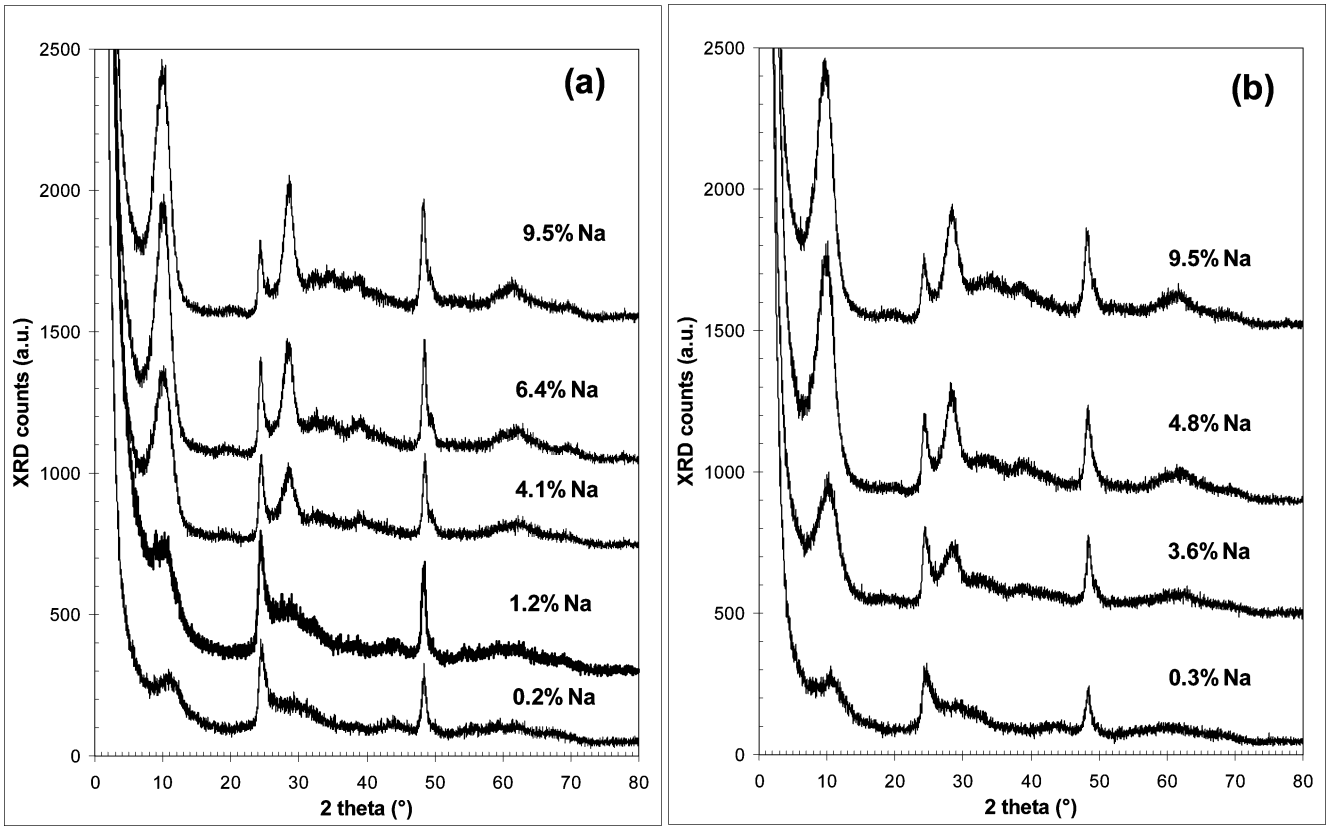

Figure 5. XRD patterns of TTNT samples synthesized from (a) A1 and (b) A2, submitted to different washing procedures (variable sodium content).

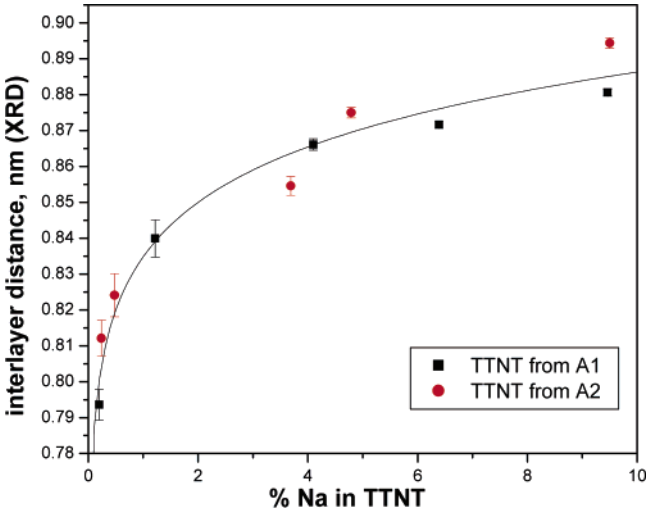

Figure 6. Dependence between interlayer distance estimated by XRD and sodium content remaining in TTNT.

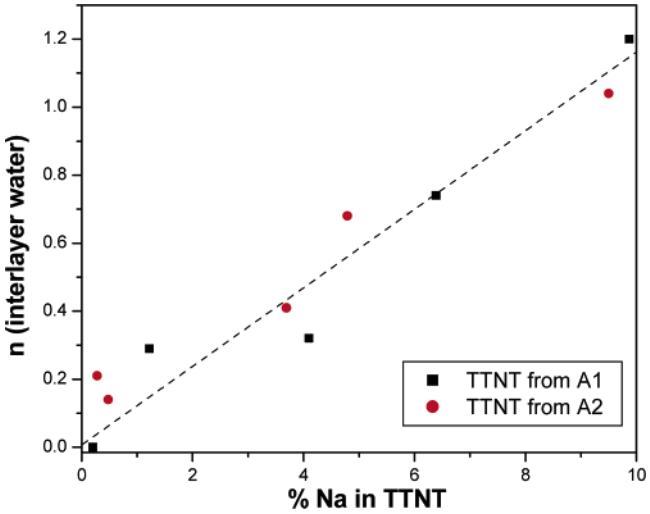

Figure 7. Dependence between interlayer water (*n*) and sodium content remaining in TTNT.

of each TTNT sample and the relative contribution of interlayer and structural water (Table 1). This revealed a correlation between the amount of interlayer water (*n*) and sodium content as displayed in Figure 7, so corroborating our previous results;[23] the present data also showed that this dependence was not influenced by the crystal size of the starting anatase (Figure 7). Although mass loss within the range of 100−500 °C varied within a narrow range (7−9%), the mass loss distribution was quite distinct. TGA plots in Figure 8 demonstrate that the higher the sodium content, the more water was released at lower temperatures, within 100−250 °C. In fact, within this range, a second endothermic event (the first appears before 100 °C due to physisorption) centered around 125−135 °C could be detected by DTA,[23] being more prominent for samples with high sodium and practically not realized for those with low sodium. This mass loss step is assigned to the interlayer water, which is released earlier than the structural hydroxyls, which need higher temperatures for complete dehydration. A small mass increase between 500 and 800 °C (<1%) was observed in most cases. We could not explain this systematic effect and assumed it as an unknown artifact. Figure 7 also suggests that extrapolation to null sodium ($x = 0$) leads to almost complete absence of interlayer water ($n = \sim 0$); this is in

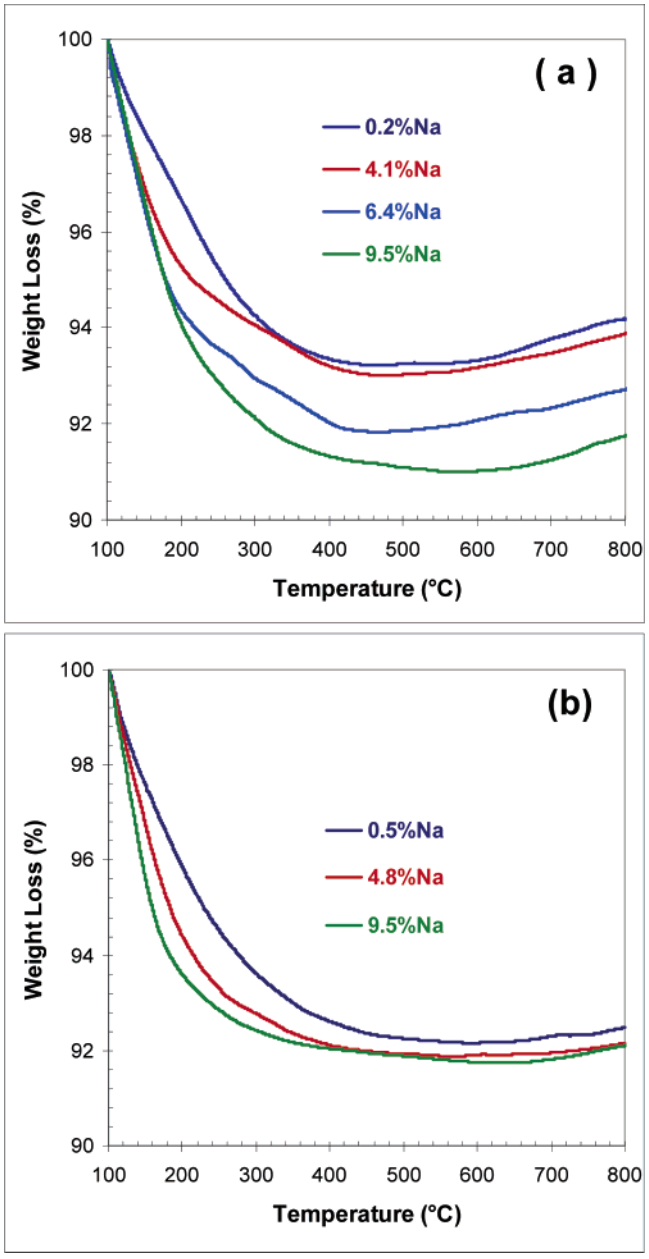

Figure 8. Relative loss of chemisorbed water determined by TGA in (a) TTNT/A1 samples and (b) TTNT/A2 samples.

very good agreement with the XRD data since interlayer distances tended to approach the *d* value of pure $H_2Ti_3O_7$ at zero sodium (Figure 6).

3.5. Textural Properties. The N_2 adsorption−desorption isotherms measured for all studied TTNT samples exhibited hysteresis loops typical of mesoporous solids. However, the shape of the hysteresis loop in TTNT was dependent both on the sodium content and mainly on the type of precursor anatase. As shown in Figure 9a, the isotherms of TTNT samples produced from A1 showed a hysteresis profile interpreted as a mix of H1 and H3 types, according to the IUPAC classification.[37] Type H1 is often related to mesoporous materials consisting of uniform pores (e.g., well-defined cylindrical-like pores) and H3 with non-rigid aggregates of plate-like particles giving rise to slit-shaped pores. On the other hand, as shown in Figure 9b, TTNT synthesized from A2 displayed hysteresis profiles much closer to a H3 type, indicating a less proportion of cylindrical pore channels and a stronger character of disordered slit-shaped pores. Isotherms in Figure 9 also evidenced smaller N_2 adsorption loads per gram of solid for samples with increasing sodium contents. The specific surface area (BET SA) of the as-synthesized TTNT samples in all cases was substantially higher than the corresponding precursor TiO_2 (as compared to A1, a 30-fold increase was noted). However, as shown in Table 2, BET SA reduced significantly with the sodium content. The decrease was steeper for the TTNTs obtained from A2.

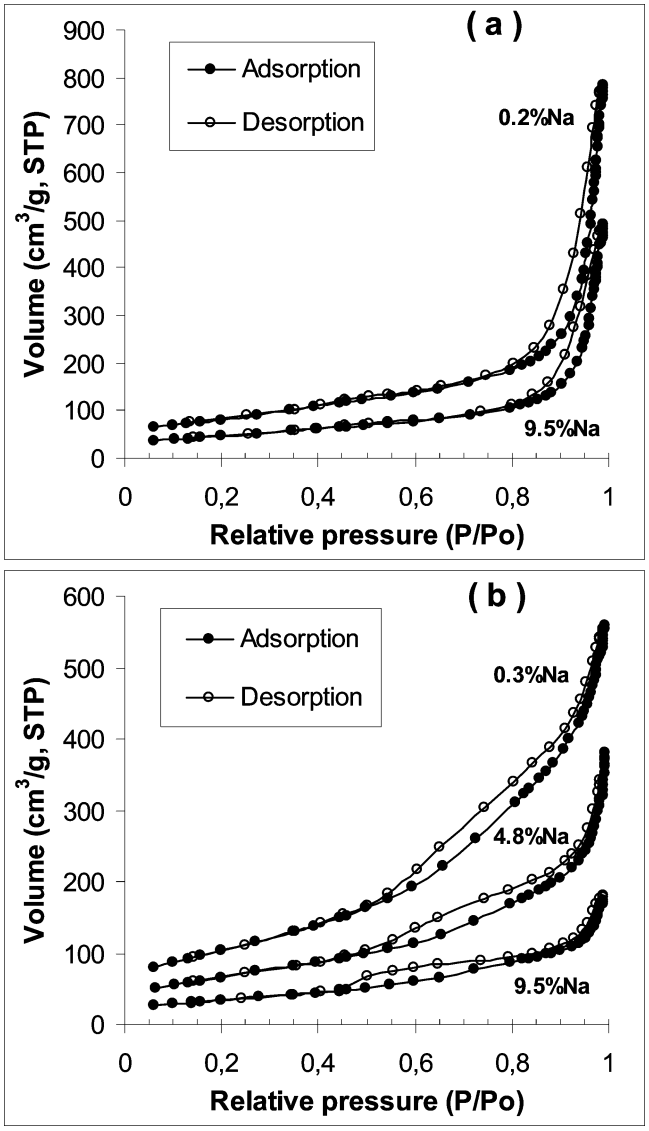

Figure 9. N_2 adsorption−desorption isotherms of (a) TTNT/A1 samples and (b) TTNT/A2 samples.

The mesopore size distributions using the BJH method derived from the N_2 desorption isotherms are shown in Figure 10. Pore volume the in *y*-axis is normalized per logarithm of pore diameter, which conventionally better represents the pore number distribution. The reliability of the pore size distribution using the BJH algorithm is restricted to the

(37) (a) Gregg, S. J.; Sing, K. S. W. *Adsorption, Surface Area, and Porosity*, 2nd ed.; Academic Press: London, 1982. (b) Lowell, S.; Shields, J. E.; Thomas, M. A.; Thommes, M. *Characterization of Porous Solids and Powders: Surface Area, Pore Size, and Density*; Kluwer Academic Publishers: Dordrecht, The Netherlands, 2004.

Table 2. BET SA and Specific Pore Volume at Different Pore Diameter Ranges as Determined from Nitrogen Adsorption Isotherms

sample/ precursor	Na (wt %)	BET SA ($m^2\ g^{-1}$)	specific pore volume ($cm^3\ g^{-1}$) 2−5 nm	5−60 nm	total (2−60)
TTNT-1/A1	0.2	289	0.105	0.630	0.735
TTNT-2/A1	1.2	316	nd	nd	nd
TTNT-3/A1	4.1	263	0.099	0.576	0.675
TTNT-4/A1	6.4	254	0.078	0.519	0.597
TTNT-5/A1	9.5	164	0.050	0.403	0.453
TTNT-1/A2	0.3	374	0.218	0.509	0.727
TTNT-2/A2	0.5	367	0.176	0.486	0.662
TTNT-3/A2	3.7	320	0.154	0.398	0.552
TTNT-4/A2	4.8	240	0.112	0.275	0.387
TTNT-5/A2	9.5	121	0.061	0.130	0.191

mesopore range displayed between 2 and 60 nm. Strong dependences on the type of precursor anatase and sodium content were found.

On TTNT-A1 samples (Figure 10a), a bimodal distribution could be distinguished: a small peak centered near 3.5 nm (inset in Figure 10a) and another one with a wide distribution ranging from 5 to 60 nm (upper limit). The specific pore volumes determined by N_2 adsorption for these two ranges are summarized in Table 2. The peak within the smaller mesopore region (2−5 nm) is supposed to correspond to the inner space of the nanotubes, while the broader mode covering the largest mesopore range accounts for the intercrystallite space generated from the aggregation of nanotubes. These assumptions are in very good agreement with low magnification TEM images showing TTNT aggregates and high magnification ones revealing individual nanotubes with inner diameters between 3 and 4 nm. SEM images also confirmed the existence of an interparticle porous structure for TTNT samples (Figure 3). Pore volume due to interaggregation was at least five times higher than the volume attributed to the nanotube inner space, although this latter contributed at least to the same extent in terms of pore area. In line with BET surface area measurements, the specific pore volume, especially within the range of 2−5 nm, increased significantly with the reduction of sodium in TTNT. This could not easily be explained by the generation of more nanotubes after an acid washing step since intense TEM observation indicated similar TTNT yields independent of sodium loading. Actually, a few titanate sheets and nanorods could be found now and then, but in a similar and very small extent for all TTNT-A1 samples. Although not evident on the limited domain analyzed by TEM, the other possibility would be a significant increase in the average internal diameter of the nanotubes as a proton substituted for sodium; however, this was not supported by the pore size distribution (i.e., position of the first peak in Figure 10a was not altered). Apart from these geometrical changes to explain the apparent dependence of the textural properties on the sodium content, one cannot forget that measured surface area and pore volume are specific (i.e., they are expressed per gram of porous solid). Therefore, even assuming the same nanotube yield and inner pore diameter, the values of specific volume can be significantly varied if skeletal density and/or the average wall thickness are changed. The skeletal density of TTNT samples should be

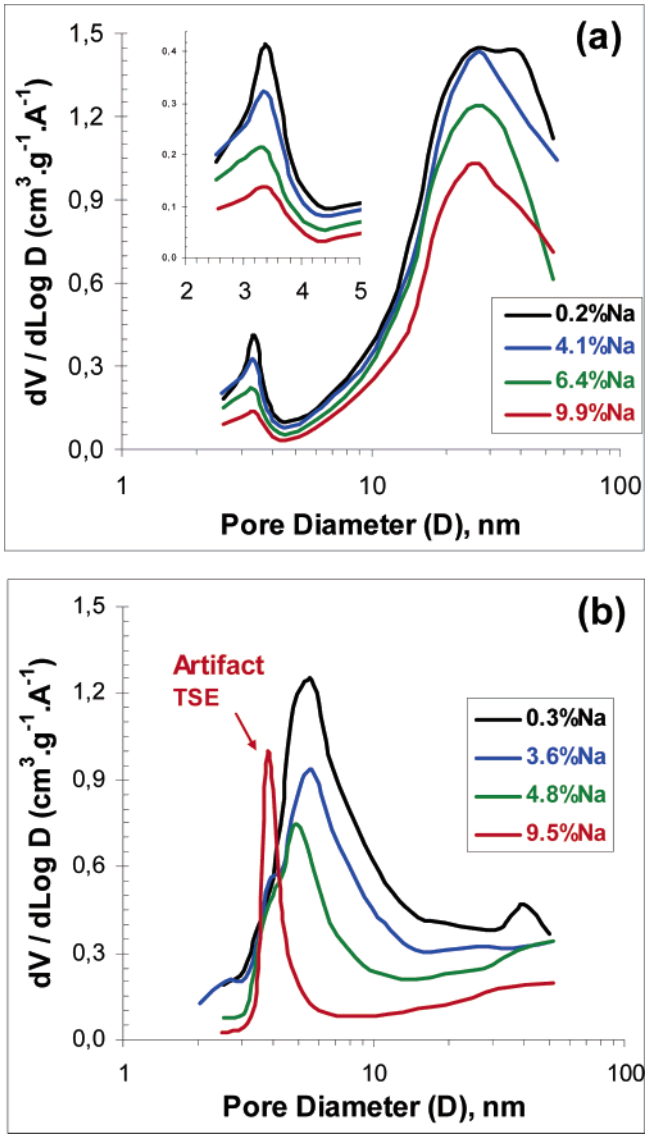

Figure 10. Pore volume distribution (BJH desorption) of (a) TTNT/A1 samples and (b) TTNT/A2 samples.

dependent on the composition $Na_xH_{2-x}Ti_3O_7{\cdot}nH_2O$ since the decrease of sodium (x) leads on one hand to a reduction in molecular weight (H replaces Na, and n is reduced) and on another hand to a contraction of the layered structure. By attributing incremental values of x between 0 and 2 as well as estimating the respective values of n and interlayer space d according to their empirical interdependence established in Figures 6 and 7, one could calculate the corresponding unit cell densities assuming the a direction (perpendicular to the layers) as the only dimension being altered in accordance with the degree of proton exchange (Figure 6). Figure 11 shows the resulting plot of calculated skeletal density versus sodium load (x). For $x = 2$, the density reaches 3.27 g cm^{-3}, slightly lower than the density of bulk $Na_2Ti_3O_7$ (known to be ~3.4 g cm^{-3}) due to the small expansion caused by intercalated water. For $x = 0$, the density approached 3.1 g cm^{-3}, which is very close to the reported density for pure $H_2Ti_3O_7$ ($\rho = 3.18$ g cm^{-3}).[38] Notice in

(38) JCPDS info. $Na_2Ti_3O_7$: 31−1329 (density: 3.441) and $H_2Ti_3O_7$: 41−0192 (density: 3.186)

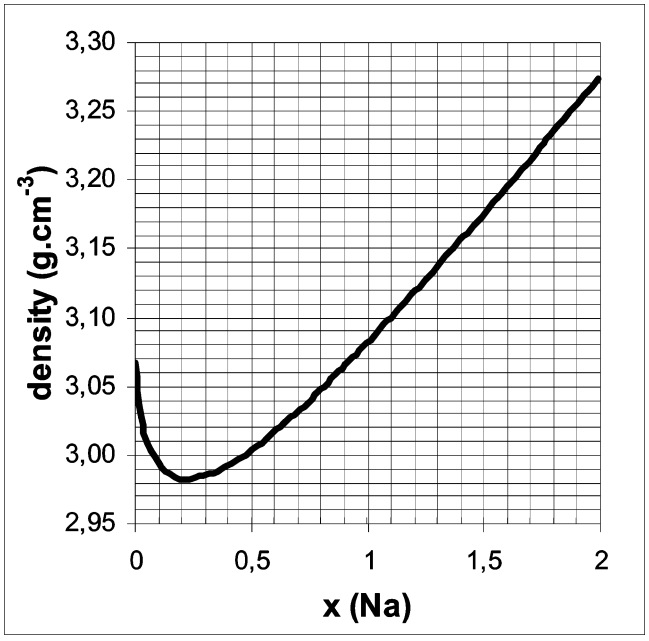

Figure 11. Calculated skeletal density of TTNT samples as a function of sodium (x) in TTNT composition $Na_xH_{2-x}Ti_3O_7 \cdot nH_2O$.

Table 3. Simulations on Calculating Specific Inner Volume of Nanotubes and Specific Surface Area (eqs 1 and 2)

case	ρ (g cm^{-3})	De (nm)	Di (nm)	r (nm)	h (nm)	V_{spec} (cm^3 g^{-1})	SA_{spec} (m^2 g^{-1})
1	3.16	8	3	1.5	2.500	0.052	253
2	3.05	8	3	1.5	2.500	0.055	262
3	3.05	7.2	3	1.5	2.100	0.069	312
4	3.05	7.2	3.5	1.75	1.850	0.101	354

Figure 11 that when replacing sodium by hydrogen down to $x = 0.2$, the density decreases steadily since the molecular weight reduction prevails over the structure compaction caused by a slight decrease in the interlayer distance; beyond this point, the drop in interlayer distance was steeper (Figure 6), and contraction was stronger, thus causing some increase in density of the solid until $x = 0$ was reached.

To assess the effects of skeletal density and average wall thickness on the pore volume, we made use of eq 1, which was deduced and allowed calculating the specific volume of pores inside tubes as a function of its geometry and density

$$V_{spec}\ (cm^3/g) = r^2/\rho[(r+h)^2 - r^2] \qquad \text{(eq 1)}$$

where ρ is the density of the solid part, r is the internal radius in nanometers of the tube, and h is the thickness (nm) of the tube wall being estimated as

$$h = 1/2[\text{external diameter } (D_e) - \text{internal diameter } (D_i)]$$

The idea was to compare the calculated V_{spec} with the experimental values obtained by N_2 adsorption within the range of 2−5 nm (Figure 10a and Table 2), which have been tentatively assigned to the intrinsic pore volume of the nanotubes in the TTNT-A1 series. In Table 3, different cases were simulated. The first one was based on the sample TTNT-5/A1 with the highest sodium content ($x = 1.4$, thus an interpolated density of 3.16) and assumed typical average dimensions of nanotubes in the TTNT-A1 series as examined by TEM: $D_e = 8$ nm and $D_i = 3$ nm. This resulted in an estimated specific volume of 0.052 cm^3 g^{-1}, which is very close to the value of 0.050 cm^3 g^{-1} measured for TTNT-5/A1 within the pore size region of 2−5 nm (Table 2) attributed to the internal pores of nanotubes. This is a strong support for our assignment. Case 2 in Table 3 was simulated to verify the separate effect of the skeletal density by simply replacing the density of TTNT-5/A1 by that of TTNT-1/A1 with the lowest sodium ($x = 0.03$ and density 3.05). This led to only a small increase in V_{spec}, not enough to explain the differences in specific pore volume (2−5 nm) between TTNT-5/A1 and TTNT-1/A1. Therefore, density is not a factor to explain all the increases in specific pore volume when exchanging sodium by a proton in the TTNT-A1 series (Table 2). Case 3 further simulated the contraction of the structure as a result of the reduction in interlayer distance when sodium was exchanged; it was assumed that there was an interlayer reduction of 0.1 nm (see Figure 6) and nanotube walls composed of four parallel interlayers, totaling a contraction of 0.8 nm represented by a reduction in the external diameter (8 → 7.2 nm) and a decrease of just 0.4 nm in the wall thickness. This resulted in a remarkable increase of V_{spec} to 0.07 cm^3 g^{-1}. A final case was figured out to demonstrate that small changes in TTNT dimensions were able to remarkably modify the specific pore volume calculated via eq 1. Starting from case 3, case 4 simulated a small change in internal diameter (D_i) from 3.0 to 3.5 nm leading to a V_{spec} of 0.101 cm^3 g^{-1}. This value coincides with the value of ∼0.1 cm^3 g^{-1} (Table 2) experimentally observed for TTNT-1 with the highest mesopore volume in the TTNT/A1 series. Therefore, the increase in pore volume measured within the 2−5 nm range when sodium was reduced from 9.5 to 0.2 wt % (Figure 10a and− Table 2) may be ascribed to a combination of reduced skeletal density, interlayer contraction (reduced wall thickness), and minor increase in internal diameter, hardly detected either by TEM or N_2 adsorption (BJH). In comparison with the pore volume change within the small mesopore range (<5 nm), the specific volume measured within the larger range (5−60 nm) was increased to a lesser extent when sodium was removed.

Specific surface area of lengthy nanotubes ($L >> r$) could also be deduced as a function of its geometry and density, as shown in eq 2.

$$SA_{spec}\ (cm^2/g) = 2 \times 10^7(2r+h)/\rho[(r+h)^2 - r^2] \quad \text{(eq 2)}$$

Assuming the same cases simulated previously, the last column of Table 3 presents the corresponding calculated surface areas. Individual observed versus calculated comparisons were not so good, but the overall range of calculated surface areas agreed reasonably well with the observed range of surface areas measured by the BET method in this series.

Another completely distinct picture regarding textural properties has been found for the TTNTs obtained from anatase of low crystal size (TTNT/A2 series). As shown in Figure 10b, a wide distribution covering all mesopore size ranges was observed with no clear evidence of bimodal distribution. While peak positions did not significantly change in TTNT/A1 series (Figure 10a), there was a clear shift of the distribution toward larger a diameter range when

sodium was reduced in the TTNT/A2 series. However, it must be pointed out that the peak narrowing noticed for the sample TTNT-5/A2 with 9.5% Na is an artifact caused by a spontaneous evaporation of the capillary condensed liquid due to the so-called tensile strength effect (TSE).[37] This phenomenon causes a steep region associated with a (forced) closure in the hysteresis loop (H3 type) at a relative pressure of ca. 0.40−0.45; indeed, this is very much the feature of the hysteresis of this sample in Figure 9b. The result is that all remaining volume to be desorbed is counted at once at this P/P_o (related to a pore diameter near 3.5 nm) giving rise to an artificial spike. Some papers dealing with pore size distribution of TTNT samples have erroneously interpreted this artifact as a real effect.[34] Despite the artifact in Figure 10b, the tendency of shift in pore size distribution as a function of the sodium content can be considered a real trend. The approach used in the TTNT/A1 series of calculating the theoretical specific surface area and specific pore volume of the nanotubes for comparison with the experimental values cannot be readily applied to this case for two basic reasons: (i) it was not evident from TEM examination that nanotubes were extensively formed in TTNT/A2 samples and (ii) the unimodal profile in the BJH pore size distribution does not allow a clear separation between pore volume due to inner space of nanotubes and those attributed to interparticle voids. Assuming that non-scrolled or non-hollowed particles prevail over nanotubes in these TTNT/A2 samples, as suggested by their TEM images and adsorption−desorption hysteresis, it is reasonable to accept that the mesopore volume in this case is mainly explained by the interspace region of the particle aggregates. The differences in pore volume as a function of sodium load should also to some extent be ascribed to the previously described factors: reduced wall density and interlayer contraction. Such effects would occur either on nanotubes or on incompletely folded/wrapped multi-shell particles. Besides, assuming thicker walls with more layers in TTNT-A2 particles (Figure 4f vs 4c), this effect could be stronger than over the TTNT-A1 cases.

3.6. Discussion on the Mechanism of TTNT Synthesis. The results so far presented indicate that chemical composition and crystal structure of TTNT products are completely distinct from their TiO_2-anatase precursor and independent of its crystallite size. On the other hand, A2 with smaller crystallites was consumed faster in reaction than A1 when submitted to the same hydrothermal conditions. These inputs strongly suggest that a dissolution−recrystallization process is involved in this alkali reaction. It is well-accepted that single- or multi-layered titanate nanosheets are formed in the recrystallization process as intermediate entities for the generation of the nanotubes either by scrolling (rolling-up) single-layer nanosheets[11,16] or by curving (wrapping) of conjoined nanosheets.[17] In fact, in our TEM examinations we could sometimes observe single- and/or multi-layered nanosheets, incompletely rolled-up or curved, coexisting with nanotubes. The overall mechanism suggested by Bavykin et al.[17] was of particular interest in discussing our results and is comprised schematically of the following steps: (i) dissolution of TiO_2 precursor; (ii) dissolution−recrystallization of nanosheets; (iii) curving of nanosheets; and (iv) washing of nanotubes.

The first step is irreversible and corresponds to the consumption of the starting TiO_2 into a soluble titanate species. In a second step, such a species would recrystallize into solid-layered titanate nanosheets under equilibrium. On the third step, Bavykin et al.[17] assumed another equilibrium with further deposition of Ti species from solution into the nanosheets, preferentially on the boundary layers, thus causing mechanical stress and leading to the curving−wrapping of the sheets. However, other studies have proposed alternative mechanisms that do not necessarily involve Ti deposition as a driving force for conversion of nanosheets into nanotubes.[10,11,16,39] Finally, the fourth step simply demonstrates the exchange of sodium ions during washing of the already formed nanotubes.

On the basis of this sequence of reaction steps, we have tried to predict the relative behavior of A1 and A2 toward TTNT formation. As expected, A2 with much smaller TiO_2 crystals disappeared earlier than A1 for the same weight of the initial anatase per volume of alkali solution at the same hydrothermal condition, thus indicating a faster dissolution rate. Therefore, the amount of soluble titanate species generated per unit of time was significantly larger in the reaction with A2. That should have accelerated the recrystallization of nanosheets (equilibrium altered) in step ii. If step iii becomes kinetically determining (i.e., the rate of nanosheet crystallization is significantly higher than the rate of their curving into nanotubes), then the formation of thicker planar entities with multiple layers would be favored before they could be easily rolled or wrapped. These intermediate entities would be naturally more rigid and difficult to be curved, thus impairing the formation of nanotubes. This mechanism seems to explain why the anatase A2 with much smaller crystallites led to lower yields of nanotubes with thicker walls (larger external diameters) than those produced from anatase A1. According to TEM examination and N_2 adsorption isotherms, the extension in reaction time with A2 from 15 to 30 h did not help on increasing significantly the yields of nanotubes to the same level as that verified for A1-derived samples, meaning that once the thicker intermediate planar titanates are formed, it is very difficult to redissolve them and break off the energy barriers involved in the curving process. We also suggest this mechanism to explain why different authors were not able to synthesize nanotubular materials from freshly precipitated amorphous TiO_2,[11,13,40] which should dissolve extremely fast under alkali hydrothermal reactions.

Except for a few exceptions, the mechanisms of nanotube formation suggested in the existing literature do not take into account the dissolution−recrystallization step as a part of the mechanism or at least as a critical step. Some papers consider direct delamination of the anatase crystals[8,11] into layered TiO_2 sheets before rolling-up, which is most unlikely since disintegration of anatase into a titanate phase is

(39) Zhang, S.; Peng, L.-M.; Chen, Q.; Du, G.; Dawnson, G.; Zhou, W. *Phys. Rev. Lett.* **2003**, *91*, 256103.
(40) Chen, Q.; Zhou, W.; Du, G.; Peng, L.-M. *Adv. Mater.* **2002**, *14*, 1208.

unquestionable evidence. Other papers suggest an acceptable mechanism, which comprises the peeling off of titanate plates formed from a disordered or fragmented raw material,[16,22,39] thus providing flexible single-layer sheets, the kinetic intermediates in the formation process of the nanotubular material. None of these proposed mechanisms, however, have considered the reactivity of the raw material as a variable. Our experimental results strongly suggest that the reactivity of TiO_2 should have an impact on the relative rate of formation of the intermediate layered titanates and has to be taken into consideration in the overall mechanism of nanotube generation.

4. Conclusion

Nanostructured materials obtained by hydrothermally reacting TiO_2-anatase with NaOH via Kasuga's method possess a trititanate-layered structure with a general formula $Na_xH_{2-x}Ti_3O_7 \cdot nH_2O$. Detailed TGA and XRD characterization indicated that the as-synthesized material rich in sodium as an interlayer cation contained a large amount of intercalated water (n), which linearly reduced with the decrease in sodium content until almost complete proton exchange, when n became nearly zero and the interlayer distance steeply decreased approaching the same interlayer distance (d_{200}) of $H_2Ti_3O_7$, thus proving consistency in our assignment. The interdependence between x, n, and d_{200} allowed for the calculation of skeletal density of the material as a function of its chemical composition.

Chemical composition and crystal structure of TTNT as well as their dependence on sodium content were not affected by the crystallite size of the starting anatase (8 vs 220 nm). On the other hand, morphology at the nanometer scale and textural properties were quite dependent on the precursor TiO_2. TEM examination and N_2 adsorption measurements identified two types of products: (i) the ones obtained from large anatase crystals (A1) displayed high yields of nanotubes with external diameters no greater than 11 nm and a pore size distribution clearly showing two contributions: one within 2−5 nm attributed to the inner space of the nanotubes and the other within 5−60 nm ascribed to the interspace between nanotubes. (ii) The ones obtained from very small anatase crystals (A2) displayed non-hollowed layered particles coexisting with less abundant nanotubes with external diameters and wall thicknesses systematically larger than those obtained from A1, while their monomodal pore size distribution did not allow separating pore volume from inner nanotube space and interparticle voids.

Differences in specific surface area and pore volume distribution as a function of the degree of proton exchange could be at least partly attributed to a combination of reduced skeletal (wall) density and interlayer contraction. It was possible to explain the dependence of textural and morphological properties on the crystal size of starting anatase based on a mechanism that considers the relative rates of dissolution−recrystallization and curving steps.

Acknowledgment. The authors are grateful to PETROBRAS S.A. for financial support. The authors thank Francisco Vieira, Andrea Pinheiro, Angelica Marques, and Darlan dos Santos from SENAI/CTGas for the XRD, TG/DTA, and SEM analyses and Denise Costa from Petrobras/CENPES for the N_2 adsorption measurements.

CM061294B